PAPER

Check for updates

High-temperature lead-free multilayer ceramic capacitors with ultrahigh energy density and efficiency fabricated *via* two-step sintering†

Ziming Cai, [ID] Chaoqiong Zhu, Hongxian Wang, Peiyao Zhao, Lingling Chen, Longtu Li and Xiaohui Wang*

The utilization of multilayer ceramic capacitors (MLCCs) in energy-storage applications is drawing increasing attention since the energy density of MLCCs has been improved significantly. However, the low dielectric breakdown strength and high loss at high temperatures are still key challenges which limit the application of MLCCs in high-voltage or high-temperature systems. In this work, a two-step sintering (TSS) method with a fast first-step heating rate of 40 °C min^{-1} is introduced to fabricate lead-free MLCCs. Compared with that of MLCCs sintered by the TSS method with a low heating rate of 4 °C min^{-1}, the interface bonding between internal metal electrodes and dielectric layers of MLCCs sintered *via* the TSS method with the fast heating rate is dramatically improved. Nearly no pores between the internal electrodes and dielectric layers or discontinuity of internal electrodes is observed. A high energy density of 8.13 J cm^{-3} and an ultrahigh efficiency of 95% are achieved under an applied electric field of 750 kV cm^{-1} in the MLCC sintered *via* the TSS method with the fast heating rate. Furthermore, this TSS method sintered MLCC exhibits a wide usage temperature range up to 170 °C, with a variation of discharge energy density less than 7%. Notably, it maintains a high efficiency over 91% even at a high temperature of 170 °C. These features demonstrate that MLCCs sintered *via* the TSS method with the fast heating rate are promising candidates for high-temperature energy-storage applications.

New energy technology is undergoing rapid development to overcome the growing environmental problems and meet the idea of sustainable development. As a result, environmentally friendly and low-cost energy-storage devices are in high demand.[1–6] Compared to batteries and electrochemical capacitors, dielectric capacitors always possess ultrahigh power density and fast charge–discharge capability, playing a crucial role in advanced pulsed power systems such as hybrid electric vehicles, high voltage pulsed-power circuits and kinetic energy weapons.[7–11] However, the low energy-storage density, low working voltage and high loss, especially at high temperatures, limit their application. Theoretically, the energy-storage performance of dielectric capacitors is dominated by the dielectric materials themselves and the structure of dielectric capacitors.[12–14] Polymer-based and ceramic-based materials are two main dielectric materials.[15,16] Polymer-based dielectrics usually have high breakdown strength and high energy-storage density; however, the low energy-storage efficiency and high heat production limit their application in high-temperature

systems.[17–19] Despite the low energy-storage density, ceramic-based dielectrics exhibit better temperature stability and thus still receive considerable attention, especially in high-temperature applications.[20–24] For example, Jia *et al.* reported a type of CaZrO$_3$ modified Bi$_{0.5}$Na$_{0.5}$TiO$_3$–NaNbO$_3$ ceramic system with ultra-wide temperature stability. In the composition of CZ10, the variation of dielectric permittivity is less than 15% spanning from −55 °C to 400 °C, with a dielectric loss lower than 0.02 between −60 °C and 300 °C.[25]

Recently, the utilization of multilayer ceramic capacitors (MLCCs) in energy-storage applications is of high interest since MLCCs possess high volumetric capacitance and are suitable for surface mounting due to their special structures.[26–29] Furthermore, the energy-storage density of MLCCs has been enhanced significantly, which makes them one of the most promising candidates for high-power energy-storage systems. A high energy density of 9.5 J cm^{-3} was reported in NBT-SBT-based MLCCs, with a high efficiency of 92% in the breakdown electric field of 720 kV cm^{-1}.[16] Wang *et al.* claimed that an ultrahigh discharge energy density of 10.5 J cm^{-3} and an efficiency of 87% have been obtained in doped BiFeO$_3$–BaTiO$_3$ ceramic multilayers.[30] However, the internal electrodes of these two types of MLCCs are Pt, which is too expensive for commercial applications. Zhao *et al.* reported a type of BTBZNT-

State Key Laboratory of New Ceramics and Fine Processing, School of Materials Science and Engineering, Tsinghua University, Beijing 100084, China. E-mail: wxh@mail.tsinghua.edu.cn

This journal is © The Royal Society of Chemistry 2019

J. Mater. Chem. A, 2019, 7, 14575–14582 | **14575**

based MLCC with a high discharge energy density of 10.12 J cm^{-3} and an efficiency of 89.4% under an electric field of 1047 kV cm^{-1}. The layer thickness of this MLCC is controlled at ~5 μm.[31] Nevertheless, the high loss at high temperatures is still a huge challenge. For example, the energy-storage efficiency of doped $BiFeO_3$–$BaTiO_3$ ceramic multilayers at 150 °C was around 70%. This low energy-storage efficiency will lead to high heat production and accelerate the failure of MLCCs. In addition, it is a type of energy waste.

The rapid development of the avionic and automotive industries, underground oil and gas exploration, advanced propulsion systems and hybrid electric vehicles has resulted in an urgent demand for high-temperature dielectric capacitors.[32] For example, in hybrid electric vehicles, the underhood temperature is always more than 140 °C. Meanwhile, the interface bonding between internal metal electrodes and dielectric layers of MLCCs and the continuity of internal electrodes are key factors that affect the dielectric breakdown strength and the energy-storage efficiency of MLCCs.[33,34] The existence of pores in the electrode and dielectric layer interface and the discontinuity of internal electrodes will both lead to the concentration of the local electric field, and this is why the probability of dielectric breakdown is greatly increased. Additionally, the concentration of the local electric field will lead to the enhancement of leakage current and further decrease the energy-storage efficiency, especially at high temperatures.

In this work, based on the advanced two-step sintering method,[35] we study the effect of the heating rate of the first-step of sintering on the microstructures and properties of energy storage MLCCs, especially to improve the quality of the interfaces between internal electrodes and dielectric layers of MLCCs by adopting a fast heating rate. As an example, the high-performance lead-free relaxor ferroelectric ceramic $0.87BaTiO_3$–$0.13Bi(Zn_{2/3}(Nb_{0.85}Ta_{0.15})_{1/3})O_3$ (BT–BZNT) is selected as the dielectric layer material of MLCCs, since this type of relaxor ferroelectric shows the highest energy efficiency.[31] Meanwhile, 60Ag/40Pd is selected as the internal electrodes to guarantee the co-sintering of ceramic dielectrics and metal electrodes and lower the cost. Each MLCC contains ten active dielectric layers with a single-layer thickness of 11 μm and an effective single layer electrode area of ~2.7 mm × 3.2 mm. The microstructure of the internal electrodes, dielectric layers and their interfaces is characterized through a Focused Ion Beam-Scanning Electron Microscope (FIB-SEM) technique.[33,36] Finally, the mechanism of the enhanced dielectric breakdown strength and the energy-storage efficiency by increasing the heating rate is modelled by a phase-field method and a leakage-current finite element method.

Three heating rates during the first-step of sintering, namely, 4 °C min^{-1}, 20 °C min^{-1}, and 40 °C min^{-1}, were adopted in our work. The corresponding fabricated MLCCs are denoted as MLCC-4, MLCC-20 and MLCC-40, respectively. The surface and cross-sectional scanning electron microscope (SEM) images of MLCCs with various first-step heating rates are shown in Fig. 1. It is clear that as the first-step heating rate increases, the grain size of the dielectric material (BT–BZNT) is reduced significantly, which contributes to the higher density of dielectric

layers. This can be confirmed in the cross-sectional SEM images in Fig. 1(d) to (f). The dielectric layers of MLCC-4 show some pores while there are no obvious pores in the dielectric layers of MLCC-40. Notably, the morphologies of internal electrodes are quite different. When the heating rate is slow during the first-step of sintering, taking 4 °C min^{-1} (MLCC-4) as an example, a large number of pores can be observed in the internal electrodes, together with some discontinuities. However, in MLCCs sintered *via* a high heating rate, *i.e.* 40 °C min^{-1} (MLCC-40), nearly no pores between the internal electrodes and dielectric layer or discontinuity of internal electrodes is observed. This can be seen more clearly in Fig. S1,† with a larger field of view. During the sintering process, a low-melting interfacial liquid alloy layer is formed when the metal electrodes are under tension. This interfacial liquid phase accelerates stress-induced diffusion and is the key cause for the formation of severe electrode discontinuities and pores between the internal electrodes and dielectric layer during heating. The formation of this interfacial liquid alloy layer can be kinetically controlled using fast-heating rates, realizing better metal electrode continuity.[37] Brennecka *et al.* have mentioned that the two-stage sintering approach described by Wang *et al.*[35] might be one approach for achieving high density in Ni–$BaTiO_3$ MLCCs with minimal electrode interactions and dewetting while retaining a fine grain size.[38]

The morphologies of internal electrodes, *i.e.* the quality of interface bonding between internal metal electrodes and dielectric layers, play a crucial role in dielectric and energy-storage performances of MLCCs. A comparison of the main energy-storage properties of MLCCs sintered with various first-step heating rates is summarized in Fig. 2. The temperature-dependent dielectric permittivity and loss are displayed in Fig. 2(a). The dielectric loss of these MLCCs sintered with various first-step heating rates is almost the same, indicating that the grain size has a small influence on the dielectric properties of these types of relaxor ferroelectrics. The difference in dielectric permittivity is mainly caused by the different area loss of the internal electrodes. There are nearly no pores in the internal electrodes of MLCCs sintered *via* the fast heating rate, leading to a small area loss of the internal electrodes, which accounts for the higher dielectric permittivity. The first-step heating rate has little influence on the relaxor behavior of the dielectric layer material, since the variation trend in temperature-dependent dielectric permittivity is almost unchanged. In terms of energy-storage performance, the hysteresis loops (P–E loops) of MLCCs sintered with various first-step heating rates are measured from a low applied electric field to their own breakdown electric field at 1 Hz, as seen in Fig. S2.† A typical comparison of hysteresis loops under an electric field of 500 kV cm^{-1} is selected and presented in Fig. 2(b). The polarization of the MLCC sintered with the fast heating rate under 500 kV cm^{-1} is slightly enhanced due to the low area loss of internal electrodes. The discharge energy density and energy efficiency as a function of the applied electric field are calculated based on the hysteresis loops in Fig. S2† and are plotted in Fig. 2(c). When the applied electric field is lower than 250 kV cm^{-1}, the energy-storage performances of all
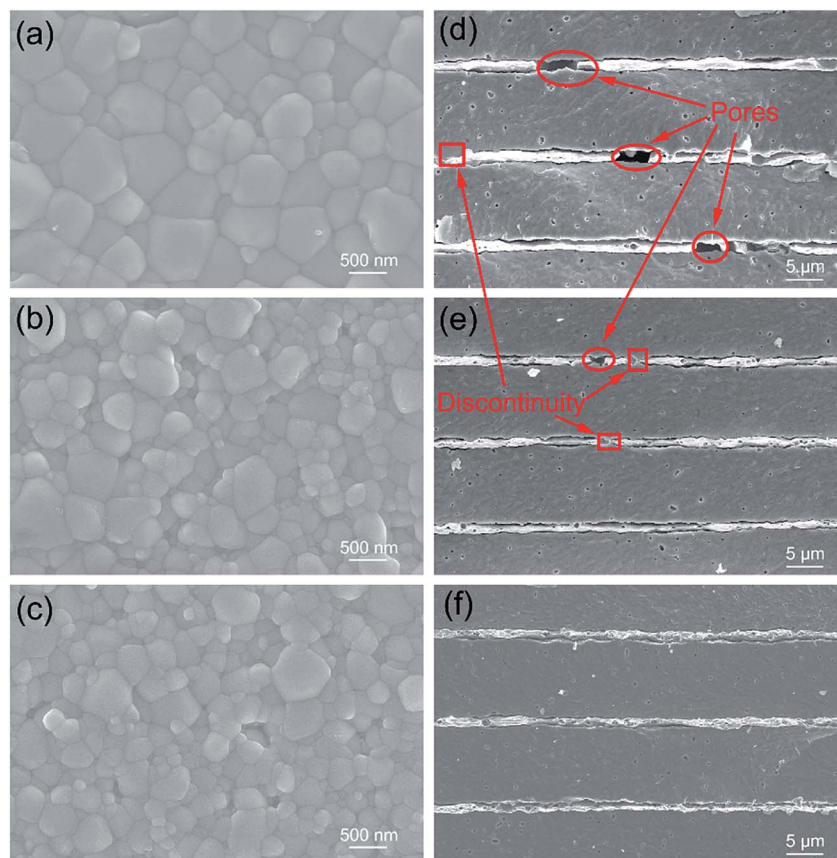
14576 | *J. Mater. Chem. A*, 2019, **7**, 14575–14582

This journal is © The Royal Society of Chemistry 2019

Fig. 1 (a) to (c) The surface SEM images of the MLCCs sintered with first-step heating rates of (a) 4 °C min^{-1}, (b) 20 °C min^{-1}, and (c) 40 °C min^{-1}. (d) to (f) The cross-sectional SEM images of the MLCCs corresponding to (a) to (c), in which the pores and discontinuity of internal electrodes can be clearly distinguished.

MLCCs are almost the same. However, as the applied electric field increases, MLCCs sintered with the fast heating rate (such as MLCC-40) display a slightly higher discharge energy density compared to that of MLCC-4 and MLCC-20, due to the larger energy efficiency. Under a higher applied field, the energy loss is mainly caused by the gradually increased leakage current, as seen in Fig. S3.† This increase of leakage current is much more serious in MLCCs with bad interface bonding between internal metal electrodes and dielectric layers, such as MLCC-4 or MLCC-20 in this work. Therefore, the energy efficiency of MLCC-4 and MLCC-20 is gradually reduced below 90% under a higher applied field, limiting their application in high-voltage systems, whereas a high energy density of 8.13 J cm^{-3} and an ultrahigh efficiency of 95% are achieved under an applied electric field of 750 kV cm^{-1} in the MLCC sintered with the fast heating rate by the TSS method (MLCC-40), which can be considered one of the most promising candidates for high-voltage applications. Fig. 2(d) summarizes the maximum discharge energy density of MLCCs sintered with various first-step heating rates. Benefiting from the improved interface bonding between internal metal electrodes and dielectric layers, the MLCC sintered with the fast heating rate by TSS exhibits a higher breakdown strength, together with a higher discharge energy density and an ultrahigh energy efficiency. The

insulation resistance of these MLCCs with various first-step heating rates is measured and presented in Table S1,† and is directly related to the breakdown strength of the MLCCs. The MLCC sintered with the fast heating rate by the TSS method (MLCC-40) shows an insulation resistivity of an order of magnitude higher than that of MLCC-4, thus exhibiting a higher breakdown strength.

High-temperature energy-storage devices are in urgent demand due to the rapid development of the avionic and automotive industries, underground oil and gas exploration, advanced propulsion systems and hybrid electric vehicles.[32] The temperature-dependent energy-storage performances of these MLCCs are further studied. The temperature-dependent discharge energy density and energy efficiency of the MLCCs sintered with various heating rates, measured under the applied field of 500 kV cm^{-1} at 1 Hz, are shown in Fig. 2(e), based on the hysteresis loops in Fig. S4.† As can be seen, the energy efficiency of MLCC-4 or MLCC-20 is gradually reduced below 80% at a high temperature of 170 °C. The leakage current is the main reason that causes energy loss at high temperatures and high applied fields as seen in Fig. S5.† Lower energy efficiency means larger heat generation and thus accelerates the failure of MLCCs. However, in terms of the MLCC sintered with the fast heating rate by the TSS method, an ultrahigh energy efficiency
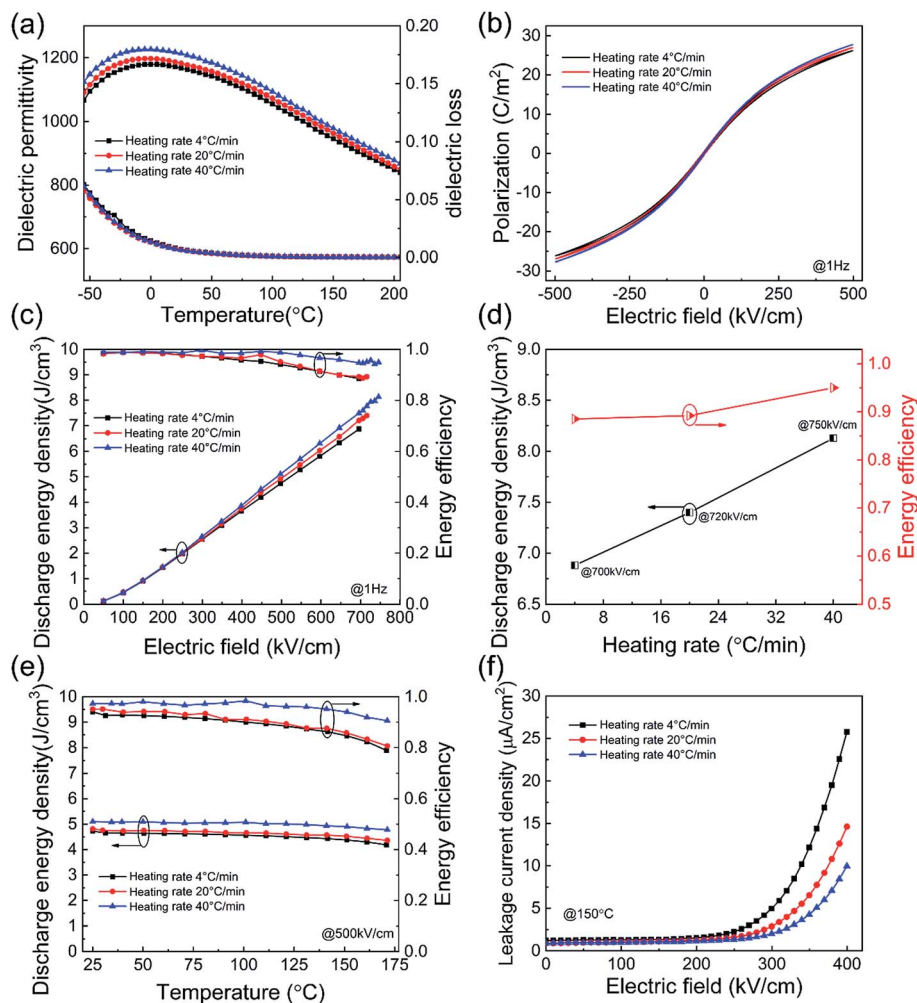
Fig. 2 (a) Temperature–dependent dielectric permittivity and loss of the MLCCs sintered with various first–step heating rates. (b) Hysteresis loops of these MLCCs measured under the electric field of 500 kV cm^{-1} at 1 Hz. (c) The calculated discharge energy density and energy efficiency of the MLCCs sintered at various heating rates as a function of the applied electric field, measured at 1 Hz. (d) The discharge energy density and energy efficiency of the MLCCs under the maximum applied field at various sintering heating rates. (e) The temperature–dependent discharge energy density and energy efficiency of the MLCCs sintered at various heating rates, measured under the applied field of 500 kV cm^{-1} at 1 Hz. (f) The leakage current density of the MLCCs as a function of the applied electric field at 150 °C.

of 91% under a high temperature of 170 °C and the high applied field of 500 kV cm^{-1} can be maintained, with a variation of discharge energy density less than 7% over the temperature range from 25 °C to 170 °C. To further confirm the leakage-current induced energy loss, the leakage current densities of these MLCCs as a function of the applied electric field at 150 °C are measured and displayed in Fig. 2(f). It is clear that the leakage current density of MLCC-4 is nearly triple that of MLCC-40.

The differences in energy-storage performances among MLCCs sintered with various first-step heating rates are closely related to their microstructures. The cross-sectional SEM images presented in Fig. 1(d) to (f) may be affected by the process of sample preparation. The cross-sectional samples are prepared through direct clipping with pliers. These SEM images might not show the original morphologies due to the intro-duced additional stress since the internal electrodes and the

dielectric layers seem to be separated. To observe the real morphologies of the internal electrodes and dielectric layers, a Focused Ion Beam-Scanning Electron Microscope (FIB-SEM) technique is adopted in our work, with the microstructure images shown in Fig. 3. Different from Fig. 1, the interface bonding between metal electrodes and the dielectric layers is quite tight. There are still many pores and discontinuity of internal electrodes existing in MLCC-4, while nearly no pores or discontinuity is seen in MLCC-40 sintered *via* the fast heating rate by the TSS method. A 3D reconstruction of the MLCC sin-tered *via* the TSS method with the fast heating rate (MLCC-40) is obtained based on 27 serial-sectional FIB-SEM images at an interval of 250 nm, with the final rendered graphics shown in Fig. 4(a). The 3D slice figure, the front sectional view and the side sectional view of the 3D reconstructed graphic of MLCC-40 are presented in Fig. 4(b) to (d), respectively. It can be confirmed that the interface bonding between the internal metal
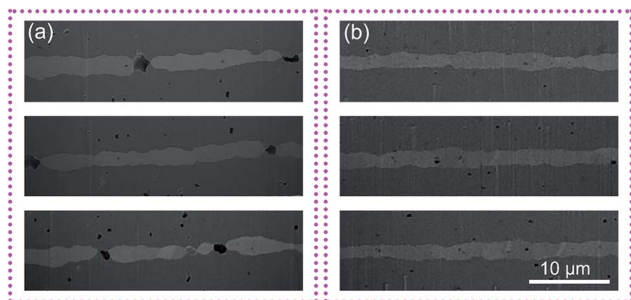
14578 | *J. Mater. Chem. A*, 2019, **7**, 14575–14582

This journal is © The Royal Society of Chemistry 2019

Fig. 3 The FIB-SEM images of internal electrodes of MLCCs sintered with first-step heating rates of (a) 4 °C min^{-1} and (b) 40 °C min^{-1}.

electrodes and dielectric layers of MLCCs sintered *via* the TSS method with the fast heating rate is dramatically improved. Nearly no pores between the internal electrodes and dielectric layers or discontinuity of internal electrodes is observed.
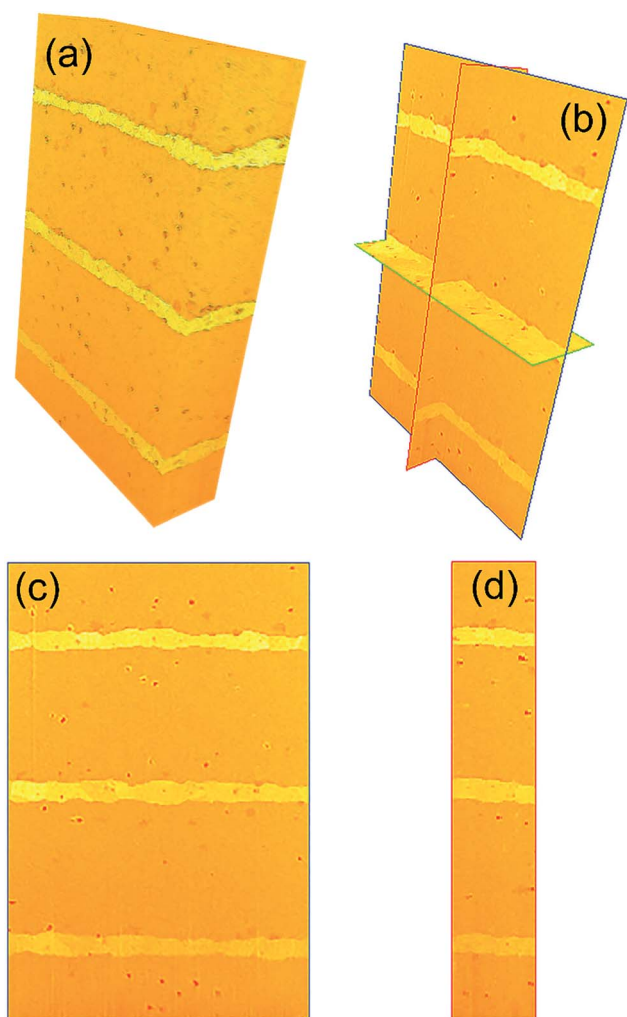

Fig. 4 (a) The 3D reconstruction with color rendered graphics of the MLCC sintered *via* the TSS method with the fast heating rate. The dark yellow represents the dielectric layers and bright yellow represents the internal electrodes. (b) to (d) The 3D slice figure (b), the front sectional view (c) and the side sectional view (d) of the 3D reconstructed graphic of (a).

The recently developed phase-field breakdown model is introduced to analyze the mechanism of the interface-quality-dependent dielectric breakdown of MLCCs.[39–41] A scalar spatially and temporally dependent damage field $s(x, t)$ is introduced to characterize the dielectric breakdown process in MLCCs. The value of continuous s varies from the intact state, $s = 1$, to the fully damaged state, $s = 0$. The effect of the size and number of pores between the internal electrodes and dielectric layers on the dielectric breakdown strength of MLCCs is studied. The final breakdown paths of MLCCs with various sizes of pores are shown in Fig. 5(a) to (f). It can be seen that in MLCCs without pores, the initiation of the breakdown path is random. Once the pores appear, the local electric field concentrates around the pores and favors the initiation of breakdown, leading to the decrease of the breakdown strength of MLCCs. As seen in Fig. 5(g) and (h), with the increase of the size and number of pores, the breakdown strength of MLCCs is gradually reduced.

The energy-storage efficiency of these MLCCs in high applied electric fields and at high temperatures is dominated by the leakage current as discussed above. To confirm this point, the local electric field distribution and leakage current density of MLCCs with various sizes and numbers of pores in the inter-faces are calculated based on a finite element method using the COMSOL Multiphysics platform.[33] The simulated distributions of the local electric field and leakage current density are illus-trated in Fig. 6(a) to (d), in which the local electric field concentrates seriously around the pores, resulting in the enhanced leakage current density. We normalize the leakage current density of MLCCs with pores to that without pores, denoted as relative current density. The effects of the size and number of pores on the leakage current density are calculated and the results are plotted in Fig. 6(e) and (f). It is clear that due to the existence of pores at the interface between the internal electrodes and dielectric layers, the leakage current density is dramatically increased. The larger the size and number of pores, the higher the leakage current. Such simulated results agree well with the experimental measurement in Fig. 2(f).

In summary, high-performance lead-free MLCCs are successfully fabricated *via* a two-step sintering (TSS) method with the fast heating rate of 40 °C min^{-1} in the first step. According to SEM and FIB-SEM images, it can be clearly seen that the interface bonding between the internal metal elec-trodes and dielectric layers of MLCCs is dramatically improved, compared to that of MLCCs sintered *via* a lower first-step heating rate. Nearly no pores between the internal electrodes and dielectric layers or discontinuity of internal electrodes is observed. Benefitting from the improved interface quality, a high energy density of 8.13 J cm^{-3} together with an ultrahigh efficiency of 95% is obtained under the applied electric field of 750 kV cm^{-1} in the MLCC sintered *via* the TSS method with a first step heating rate of 40 °C min^{-1}. Further, this MLCC exhibits excellent high-temperature energy-storage perfor-mance up to 170 °C, with a variation of discharge energy density less than 7%. Most importantly, it maintains an energy-storage efficiency higher than 91% over the temperature range from 25 °C to 170 °C. The phase-field breakdown simulation and
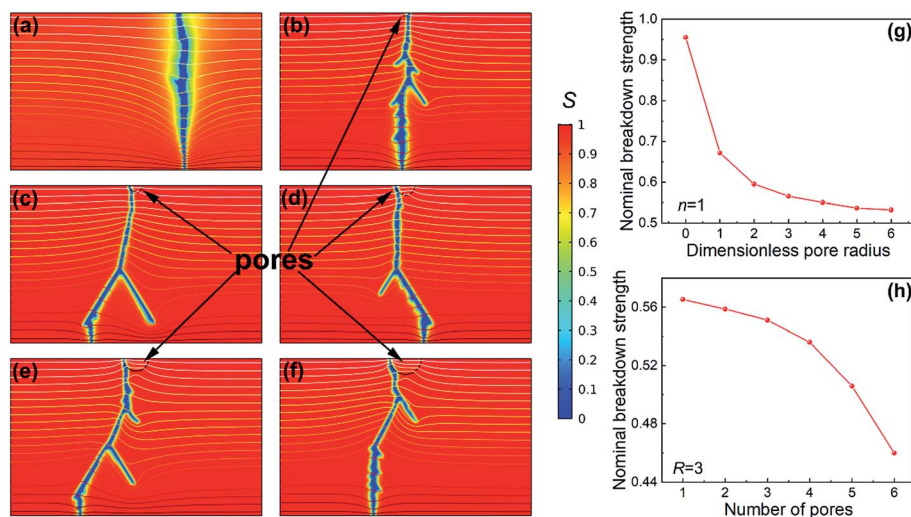
Fig. 5 (a) to (f) The final patterns of the breakdown path of the MLCCs with various dimensionless pore radii of (a) 0, (b) 1, (c) 2, (d) 3, (e) 4, and (f) 5. The shading represents the electrical treeing field variable s, with $s = 1$ indicating the intact state and $s = 0$ indicating the electrical treeing state. (g) and (h) The nominal breakdown strength of the MLCCs as functions of (g) the dimensionless pore radius and (h) number of pores.

calculated distribution of the local electric field and leakage current density based on the finite element method reveal the mechanism of the enhancement of the breakdown strength and energy efficiency of the TSS method sintered MLCCs. A good quality interface bonding without pores and discontinuity of internal electrodes contributes to the uniform distribution of the local electric field and decreases the leakage current density, leading to an enhancement in the breakdown strength and energy-storage efficiency of MLCCs. This TSS approach with the fast first-step heating rate is not only applied in BTBZNT-based MLCCs, but is also expected to be used for all types of energy-storage MLCCs, improving the interface bonding between the internal electrodes and dielectric layers and enhancing the high-voltage and high-temperature energy-storage performances.

Experimental section

Phase-field breakdown model

Inspired by the phase-field model of brittle fracture, a spatially and temporally dependent damage field $s(x, t)$ is introduced to characterize the breakdown process of these MLCCs.[39–41] The value of s varies from 1 to 0, representing the intact state and the fully damaged state, respectively. For any other intermediate state, the permittivity is interpolated using

$$\varepsilon(s) = \frac{\varepsilon^0}{f(s) + \eta}, \tag{1}$$

where $f(s) = 4s^3 - 3s^4$ and ε^0 is the initial permittivity. The governing equations for the dielectric breakdown are:

$$\nabla \cdot [\varepsilon(s)\nabla\phi] = 0, \tag{2}$$

$$\frac{1}{m}\frac{\partial s}{\partial t} = \frac{\varepsilon'(s)}{2}\nabla\phi \cdot \nabla\phi + W_c f'(s) + \frac{\Gamma}{2}\nabla^2 s, \tag{3}$$

where ϕ is the electric potential, m is the breakdown mobility, t is the time, W_c is the critical density of electrostatic energy, and Γ is the breakdown energy. The detailed procedure for solving eqn (2) and (3) can be found in the ESI,† and the whole modeling is performed on the COMSOL Multiphysics platform.

Simulation of electric field distribution and leakage current density

The distributions of the local electric field are calculated using Gauss' law:

$$\nabla \cdot D = 0, \tag{4}$$

and the constitutive relation between the electric displacement (D) and electric field (E) is given as $D = \varepsilon_0\varepsilon_r E$, where ε_0 and ε_r are the vacuum permittivity and the relative permittivity of the dielectric material, respectively. It is known that the leakage current density (J) in MLCCs is governed by the Schottky barrier at the metal–dielectric interface and is given as:[33]

$$J = AT^2 \exp\left(\frac{\alpha E^{1/2} - \varphi_0}{k_B T}\right), \tag{5}$$

where A is the Richardson constant, α is a constant dependent on the relative permittivity ε_r, k_B is the Boltzmann constant, φ_0 is the zero-bias Schottky barrier height, and T and E are the temperature and electric field, respectively. Eqn (4) and (5) are solved through the COMSOL Multiphysics platform as well.

Fabrication of 0.87BaTiO₃–0.13Bi(Zn₂/₃(Nb₀.₈₅Ta₀.₁₅)₁/₃)O₃ (BT–BZNT)-based multilayer ceramic capacitors

Based on the high energy-storage performance of BT–BZNT ceramics, BT–BZNT powders were chosen as the raw material for the dielectric layer material with an average grain size of 100 nm.[31] The weighed powders with dispersant, binder, and plasticizer were milled using zirconia balls for 48 h. Then, the

14580 | *J. Mater. Chem. A*, 2019, **7**, 14575–14582

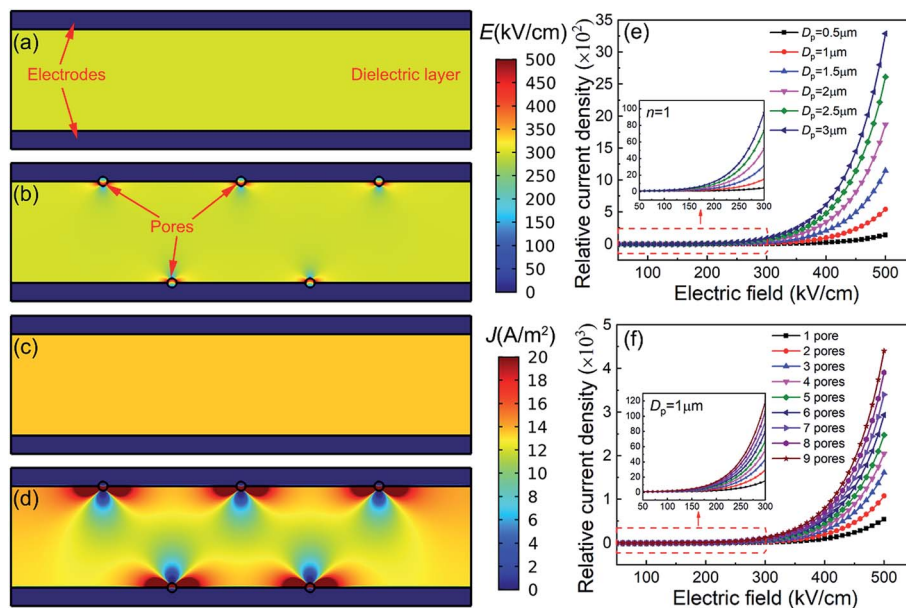This journal is © The Royal Society of Chemistry 2019

Fig. 6 (a) and (b) The simulated distribution of the electric field inside the dielectric layer of the MLCCs with (a) no pores and (b) several pores at the interface of the internal electrodes and dielectric layers. (c) and (d) The simulated distribution of current density inside the dielectric layer of the MLCCs corresponding to (a) and (b). (e) and (f) The relative current density of the MLCCs as a function of the applied electric field with various (e) diameters and (f) numbers of pores.

slurry was used to fabricate continuous BT–BZNT tapes with a thickness of about 17 μm by roll-to-roll tape-casting. The ceramic tapes screen-printed with 60Ag/40Pd paste as the internal electrodes were stacked layer by layer and precisely aligned using isostatic lamination with ten active dielectric layers. After burnout of the binder at 600 °C for 2 h, the MLCCs were sintered by a two-step sintering method with a first-step temperature of 1180–1200 °C for 1 min and cooling to the second low temperature of 1000–1040 °C for a further 3 h, as shown in Fig. S6, ESI.† First-step heating rates of 4 °C min^{-1}, 20 °C min^{-1}, and 40 °C min^{-1} were adopted in this work. After sintering, the thickness of the single active dielectric layer is ~11 μm, with an effective single layer electrode area of ~2.7 mm × 3.2 mm. Finally, Ag paste was used to terminate the opposite ends of MLCCs for further electrical property measurements.

Characterization of the microstructure and electrical properties

The surface and cross-sectional microstructures of these MLCCs were observed using a scanning electron microscope (MERLIN VP Compact, Zeiss Ltd, Germany). The temperature-dependent dielectric permittivity and loss were measured in the temperature range of from – 55 to 200 °C at 1 kHz using an impedance analyzer (HP4278A; Hewlett-Packard) with an auto-mated temperature controller (Delta Design 9023, Cohu Semi-conductor Equipment Group). The hysteresis loops and leakage current density were measured with a TF ANALYZER 2000E ferroelectric measurement system at 1 Hz (aixACCT Systems GmbH, Aachen, Germany). The serial-sectional microstructures were mechanically polished and ion beam-milled using a FIB-

SEM (Crossbeam 340, Zeiss Ltd, Germany) with a 30 kV/7 Na Ga^{3+} beam.

Conflicts of interest

There are no conflicts to declare.

Acknowledgements

References

1 K. Zou, Y. Dan, H. Xu, Q. Zhang, Y. Lu, H. Huang and Y. He, *Mater. Res. Bull.*, 2019, **113**, 190–201.

2 H. Nazir, M. Batool, F. J. Bolivar Osorio, M. Isaza-Ruiz, X. Xu, K. Vignarooban, P. Phelan, Inamuddin and A. M. Kannan, *Int. J. Heat Mass Transfer*, 2019, **129**, 491–523.

3 Q. Liu, J. Zhu, L. Zhang and Y. Qiu, *Renewable Sustainable Energy Rev.*, 2018, **81**, 1825–1858.

4 F. Li, J. Zhai, B. Shen and H. Zeng, *J. Adv. Dielectr.*, 2018, 1830005, DOI: 10.1142/s2010135x18300050.

5 K. Bi, M. Bi, Y. Hao, W. Luo, Z. Cai, X. Wang and Y. Huang, *Nano Energy*, 2018, **51**, 513–523.

6 L. Yang, X. Kong, F. Li, H. Hao, Z. Cheng, H. Liu, J.-F. Li and S. Zhang, *Prog. Mater. Sci.*, 2019, **102**, 72–108.

7 A. L. Young, G. E. Hilmas, S. C. Zhang and R. W. Schwartz, *J. Mater. Sci.*, 2007, **42**, 5613–5619.

This journal is © The Royal Society of Chemistry 2019

J. Mater. Chem. A, 2019, **7**, 14575–14582 | **14581**

8 Z. Cai, X. Wang, B. Luo, W. Hong, L. Wu and L. Li, *J. Am. Ceram. Soc.*, 2018, **101**, 1607–1615.

9 X. Zhang, Y. Shen, Q. Zhang, L. Gu, Y. Hu, J. Du, Y. Lin and C. W. Nan, *Adv. Mater.*, 2015, **27**, 819–824.

10 K. Han, Q. Li, C. Chanthad, M. R. Gadinski, G. Zhang and Q. Wang, *Adv. Funct. Mater.*, 2015, **25**, 3505–3513.

11 Q. Li, K. Han, M. R. Gadinski, G. Zhang and Q. Wang, *Adv. Mater.*, 2014, **26**, 6244–6249.

12 Z. Cai, X. Wang, B. Luo, W. Hong, L. Wu and L. Li, *J. Am. Ceram. Soc.*, 2018, **101**, 1607–1615.

13 Z. Cai, X. Wang and L. Li, *Adv. Theory Simul.*, 2019, **2**, 1800179.

14 Z. Cai, X. Wang, B. Luo, L. Wu and L. Li, *Ceram. Int.*, 2017, **43**, 12882–12887.

15 Z. Yao, Z. Song, H. Hao, Z. Yu, M. Cao, S. Zhang, M. T. Lanagan and H. Liu, *Adv. Mater.*, 2017, **29**, 1601727.

16 J. Li, F. Li, Z. Xu and S. Zhang, *Adv. Mater.*, 2018, **30**, 1802155.

17 Y. Wang, L. Wang, Q. Yuan, Y. Niu, J. Chen, Q. Wang and H. Wang, *J. Mater. Chem. A*, 2017, **5**, 10849–10855.

18 T. Zhang, W. Li, Y. Zhao, Y. Yu and W. Fei, *Adv. Funct. Mater.*, 2018, **28**, 1706211.

19 Z.-H. Shen, J.-J. Wang, J.-Y. Jiang, Y.-H. Lin, C.-W. Nan, L.-Q. Chen and Y. Shen, *Adv. Energy Mater.*, 2018, **8**, 1800509.

20 Q. Yuan, F. Yao, Y. Wang, R. Ma and H. Wang, *J. Mater. Chem. C*, 2017, **5**, 9552–9558.

21 W. Jia, Y. Hou, M. Zheng and M. Zhu, *J. Alloys Compd.*, 2017, **724**, 306–315.

22 D. Hou, T.-M. Usher, H. Zhou, N. Raengthon, N. Triamnak, D. P. Cann, J. S. Forrester and J. L. Jones, *J. Appl. Phys.*, 2017, **122**, 064103.

23 R. Muhammad, Y. Iqbal, I. M. Reaney and C. Randall, *J. Am. Ceram. Soc.*, 2016, **99**, 2089–2095.

24 W. Jia, Y. Hou, M. Zheng, Y. Xu, M. Zhu, K. Yang, H. Cheng, S. Sun and J. Xing, *IET Nanodielectric*, 2018, **1**, 3–16.

25 W. Jia, Y. Hou, M. Zheng, Y. Xu, X. Yu, M. Zhu, K. Yang, H. Cheng, S. Sun and J. Xing, *J. Am. Ceram. Soc.*, 2018, **101**, 3468–3479.

26 C. Groh, K. Kobayashi, H. Shimizu, Y. Doshida, Y. Mizuno, E. A. Patterson and J. Rödel, *J. Am. Ceram. Soc.*, 2016, **99**, 2040–2046.

27 J. Bultitude, L. Jones, B. Xu, J. Magee and R. Phillips, *IEEE 3D-PEIM*, 2016.

28 X. Xu, A. S. Gurav, P. M. Lessner and C. A. Randall, *IEEE Trans. Ind. Electron.*, 2011, **58**, 2636–2643.

29 Z. Sun, C. Ma, M. Liu, J. Cui, L. Lu, J. Lu, X. Lou, L. Jin, H. Wang and C.-L. Jia, *Adv. Mater.*, 2017, **29**, 1604427.

30 G. Wang, J. Li, X. Zhang, Z. Fan, F. Yang, A. Feteira, D. Zhou, D. C. Sinclair, T. Ma, X. Tan, D. Wang and I. M. Reaney, *Energy Environ. Sci.*, 2019, **12**, 582–588.

31 P. Zhao, H. Wang, L. Wu, L. Chen, Z. Cai, L. Li and X. Wang, *Adv. Energy Mater.*, 2019, **9**, 1803048.

32 Q. Li, F.-Z. Yao, Y. Liu, G. Zhang, H. Wang and Q. Wang, *Annu. Rev. Mater. Res.*, 2018, **48**, 219–243.

33 M. M. Samantaray, A. Gurav, E. C. Dickey, C. A. Randall and W. Y. Ching, *J. Am. Ceram. Soc.*, 2012, **95**, 264–268.

34 M. M. Samantaray, A. Gurav, E. C. Dickey, C. A. Randall and W. Y. Ching, *J. Am. Ceram. Soc.*, 2012, **95**, 257–263.

35 X. H. Wang, X. Y. Deng, H. L. Bai, H. Zhou, W. G. Qu, L. T. Li and I. W. Chen, *J. Am. Ceram. Soc.*, 2006, **89**, 438–443.

36 Z. Yan, O. Guillon, C. L. Martin, S. Wang, C.-S. Lee, F. Charlot, D. Bouvard and C. A. Randall, *J. Am. Ceram. Soc.*, 2015, **98**, 1338–1346.

37 A. V. Polotai, G.-Y. Yang, E. C. Dickey and C. A. Randall, *J. Am. Ceram. Soc.*, 2007, **90**, 3811–3817.

38 G. L. Brennecka, J. F. Ihlefeld, J.-P. Maria, B. A. Tuttle and P. G. Clem, *J. Am. Ceram. Soc.*, 2010, **93**, 3935–3954.

39 K. C. Pitike and W. Hong, *J. Appl. Phys.*, 2014, **115**, 044101.

40 Z. Cai, X. Wang, B. Luo, W. Hong, L. Wu and L. Li, *Compos. Sci. Technol.*, 2017, **151**, 109–114.

41 Z. Cai, X. Wang, B. Luo, W. Hong, L. Wu and L. Li, *Compos. Sci. Technol.*, 2017, **145**, 105–113.

14582 | *J. Mater. Chem. A*, 2019, **7**, 14575–14582

This journal is © The Royal Society of Chemistry 2019